

An Arbitrarily Accurate Algorithm for the Start up Channel Flow with Slip

Gründing, D.*¹, Raju, S.¹, and Marić, T.¹

¹*Institute for Mathematical Modeling and Analysis, TU Darmstadt, Germany*

Abstract

The transient Couette and Poiseuille channel flow solutions with different Navier slip conditions on the wall boundaries require the solution of a non-linear root-finding problem. A novel algorithm is developed that automates the computation of these roots with arbitrary precision and for general input parameters. The obtained results show a significant improvement to available coefficient values for this analytic solution. A parameter variation for the slip lengths reveals a new power law for the first series coefficient that governs the stability of the solution and is essential for slip length computations from molecular dynamics simulations. Based on the new algorithm, the time scales for the asymptotic approach to the stationary solution are quantified. A double-precision implementation and an arbitrary precision implementation provide a fast, verified, and highly accurate method to obtain benchmark quality reference solutions or a module for more general applications.

Abbreviations

APA: arbitrary precision arithmetic

CFD: computational fluid dynamics

DNS: direct numerical simulation

MEMS: micro-electro-mechanical systems

MD: molecular dynamics

PDE: partial differential equation

SCC: start-up coefficient computation

*Corresponding author. Email: gruending@mma.tu-darmstadt.de

1 Introduction

The Navier slip boundary condition is often applied in widely different contexts. For example, below a certain length scale standard assumptions for the interaction between a liquid and a solid, specifically the no slip condition, breaks down. Usually, it is replaced with a Navier type boundary condition to account for the occurring slip at the liquid solid interface [10]. Similarly, different thermodynamic conditions such as an increase in temperature can lead to an increased slip at the liquid solid interface which is again modeled using the Navier slip condition [4, 9]. In these cases, the Navier boundary condition is used to model the direct interaction between a liquid and solid phase. In contrast, on larger scales the Navier slip boundary condition is applied to model numerous different physical effects, e.g., the influence of rough or porous surfaces [22], rarefied gases [19, 2], chemically treated hydrophobic surfaces [21] dense particulate emulsions (suspensions, foams, polymer solutions) [24] including blood, and sometimes in the context of micro-electro-mechanical systems (MEMS) [10, 9, 7]. More prominently, the Navier slip boundary condition has been suggested to resolve the contact line paradox for wetting problems. The application of this boundary condition at the contact line allows in principle a solution of the continuum description for wetting phenomena [12]. However, in general the problem is more intricate, see, e.g., [20] for a more detailed discussion. Furthermore, the Navier slip boundary condition is frequently used to model the liquid-wall interaction in viscoelastic flows where the linear slip condition is extended to a memory or logarithmic slip condition [1, 23].

The application of slip boundary conditions also extend to the atomic scale. For example Majumder et al. [15] produced membranes composed of an array of aligned nanotubes and measured that flow through this array is four or five orders of magnitudes faster than would be predicted from convectional flow theory. They conclude that that these high flow rates can be attributed to a basically frictionless surface at the carbon/nanotube walls.

The direct experimental quantification of slip between a fluid and a solid poses a challenging task, as the slip length with respect to a Navier slip boundary condition are assumed to be between ångstrom and ten nanometer. In this context, Qian, Wang, and Sheng [18] used molecular dynamics (MD) simulations to approximately quantify the value of the slip length at a three phase moving contact line. Chen et al. [8], compute a continuum mechanical slip length from MD-data based on the start-up solution with slip. This allows to compute a boundary layer thickness independently from the channel height and bin sizes which typically have a strong influence on the actual value of such computations.

For a general domain geometry, a solution of the continuum model is usually obtained using tools from computational fluid dynamics (CFD). However, analytic solutions are available for the transient flow with no slip boundary conditions on the solid walls in a variety of basic geometries. Examples include the start-up flow between two parallel plates or within a pipe [5]. Such solutions are usually obtained using Laplace or Fourier transforms and typically lead to solutions in the form of infinite series.

Recently, Matthews and Hastie [16] derived the analytic solution for the two-dimensional, pressure-driven start-up velocity field in a channel with two different slip length on the opposite sides of the channel which is based on a Fourier series approach. For a single selected case, they validate their analytic solution with numerical simulations of a start-up flow using COMSOL.

Kaoullas and Georgiou [14] derived analytic series solutions for the planar and axis-symmetric case and the circular Couette flow of Newtonian fluids for a slip boundary condition with memory. It is reported that these types of slip boundary conditions lead to increased characteristic time scale in comparison to the constant slip condition regarding the development of the slip velocity at the boundary. Abou-Dina et al. [1] consider the start-up Couette flow of a Newtonian fluid for a memory Navier slip boundary condition in the context of polymer flows. It is observed that both parameters of the used memory slip boundary condition increase the characteristic time in comparison to the case with no slip boundary conditions. An analog observation for the slip length to length scale ratio has been observed in [2] (there the ratio is the Knudsen number).

Analytic solutions are applied in a variety of different applications: They prove useful for the verification and convergence studies for the numerical solution of partial differential equations. For example John [13] and Matthews and Hastie [16] use a slip flow to verify the discretization of Navier slip boundary conditions for a finite element method. Avramenko, Tyrinov, and Shevchuk [2, 3] successfully compared to Lattice-Boltzmann-simulations for the start-up flow with slip. We note that the analytic solutions can also be used as a basis to investigate the interaction between slip and heat conduction in start-up flows [7] or can be combined into phenomenological models to describe more complex phenomena such as the rise of liquid in capillaries [11].

Even though Navier slip boundary conditions and the corresponding analytic solutions have countless applications, analytic solutions are often computed manually. The series coefficients are computed for selected cases “by hand” - a tedious and error prone task as we shall see below. Furthermore, even though the start-up solution is frequently used as reference or at largely different length scales, a consideration of the overall solution accuracy is typically not available. As will be shown further below, the problem becomes relevant for large ratios of slip length to the channel length scale (e.g. channel radius). This problem becomes particularly relevant in the context of wetting, where the slip length at the contact line is usually several orders of magnitude smaller than the length scale of the overall flow. To avoid an unnecessary resolution of such small scales an accurate computation of the series solution is required.

In this work, a novel automated and robust algorithm is developed that provides reliable and arbitrarily accurate velocity fields for the start-up solution with slip, even for extreme slip length to channel width ratios. The proposed algorithm significantly simplifies the verification of numerical codes and enables an automatic quantification of slip lengths from MD-simulations as in [8].

In Section 2 the series solution for a starting channel flow with slip boundary conditions is recalled. Section 3 introduces the algorithm that solves the

non-linear characteristic equation for the flow of a liquid between two plates. While the considered characteristic equation is also relevant for a Couette flow setup we concentrate on the Poiseuille flow case. For a cross-comparison, two implementations of the algorithm are provided: one in python using a double-precision floating point representation and second C++-based implementation utilizing arbitrary precision arithmetic (APA). Both implementations are verified against full direct numerical results in Section 4. Highly accurate coefficients for a broad variety of slip lengths can be found in Appendix A.

2 Mathematical model

2.1 Channel flow with non-equal wall slip

In the following, we consider the starting flow of an incompressible Newtonian liquid with constant temperature which is moving between two infinitely extended parallel plates. The origin of the coordinate system is placed in the center of the channel where the x -coordinate points in the direction of the flow and the y coordinate is orthogonal to the channel walls. Note that a different choice of coordinate systems leads to a different form of the solution and a slightly different characteristic equation to be solved for the series coefficients. The overall algorithm developed below can also be adapted for this difference, though in the following, we will consider the case with a coordinate system in the center of the channel. We consider a Stokes flow regime leading to

$$\rho \partial_t u = \mu \partial_{yy} u + G \quad (1)$$

for the momentum conservation equation. The velocity u is pointing in channel direction, ρ is the liquid density, μ is the dynamic viscosity of the liquid and $G = -\nabla p$ is the constant pressure gradient in x direction. As initial conditions

$$u = 0 \quad \text{at} \quad t = 0 \quad \text{for} \quad -R \leq y \leq R \quad (2)$$

are used. At both wall boundaries, a Navier slip boundary condition

$$\mp L^\pm \partial_y u = u \quad \text{at} \quad y = \pm R \quad \text{for} \quad t \geq 0 \quad (3)$$

is applied. For both slip lengths, we have $L^\pm \geq 0$.

To reduce the number of parameters and represent the results in the following sections in compact format, we scale Eq. (5) as well as the initial and boundary conditions Eq. (7) by introducing the following dimensionless variables

$$u^* = u / \frac{GR^2}{2\mu}, \quad y^* = y/R, \quad t^* = t / \frac{\rho R^2}{\mu}, \quad S_\pm = L^\pm / R, \quad (4)$$

Here, u^* is the velocity, y^* is the cross section coordinate, t^* is time and the slip lengths are described by the parameters S_\pm , which all are dimensionless. This yields the dimensionless form of Eq. (1)

$$\partial_t^* u^* = \partial_{y^* y^*} u^* + 2 \quad (5)$$

with initial and boundary conditions

$$u^* = 0 \quad \text{at} \quad t^* = 0 \text{ for } -1 \leq y^* \leq 1, \quad (6)$$

$$\mp S_{\pm} \partial_{y^*} u^* = u^* \quad \text{at} \quad y^* = \pm 1 \text{ for } t^* \geq 0. \quad (7)$$

From here on we drop the *-notation and assume that we only deal with dimensionless quantities if not stated otherwise.

A series solution of Eq. (5), Eq. (6), and Eq. (7) is, e.g., available in [16]. The full solution is split into a stationary and transient contribution \bar{u} and \tilde{u} , respectively, in the form

$$u(t, y) = \bar{u}(y) - \tilde{u}(t, y). \quad (8)$$

The stationary solution \bar{u} is given by

$$\bar{u}(y) = \frac{3(S_+ + S_-) + 4S_+S_- + 2}{S_+ + S_- + 2} - \frac{2(S_- - S_+)}{S_+ + S_- + 2}y - y^2 \quad (9)$$

and the transient part can be obtained using separation of variables yielding

$$\tilde{u}(t, y) = \sum_{n=1}^{\infty} A_n (\sin(k_n(y+1)) + S^- k_n \cos(k_n(y+1)) \exp(-k_n^2 t)). \quad (10)$$

Here, the series coefficients have been scaled by $k_n^* = k_n R$, and the asterisk has been omitted as above. The formula for the coefficient A_n from Matthews and Hastie [16] can be significantly simplified by multiple insertion of the characteristic equation Eq. (12), yielding

$$A_n = \frac{8 \sin(k_n) (\sin(k_n) + S_- k_n \cos(k_n)) (k_n^2 S_+^2 + 1)}{k_n^3 (2S_+^2 S_-^2 k_n^4 + (S_+^2 (S_- + 2) + S_-^2 (S_+ + 2)) k_n^2 + S_+ + S_- + 2)}. \quad (11)$$

Note that A_n explicitly depends on S_+ , S_- , and k_n . In contrast, no such explicit formula for the coefficients k_n is available. These coefficients have to be obtained from the zeros of the non-linear characteristic equation which is

$$(1 - S_+ S_- k^2) \sin(2k) + k(S_+ + S_-) \cos(2k) = 0 \quad (12)$$

In [16] a characteristic equation is provided in the form

$$\tan(2k) - \frac{k(S^+ + S^-)}{k^2 S^+ S^- - 1} = 0. \quad (13)$$

However, as shown below, this form of the equation is not applicable in the general case. Note that the solutions of Eq. (12) are also required for the analytic start up solution in a Couette flow setup [17]. We also give a factorization of the characteristic equation Eq. (12) to be used below:

$$\begin{aligned} & (\cos k - S_+ k \sin k)(\sin k + S_- k \cos k) \dots \\ & \dots + (\cos k - S_- k \sin k)(\sin k + S_+ k \cos k) = 0. \end{aligned} \quad (14)$$

In the following, we review several special cases of the general flow considered above. These are used as reference solutions in the results section.

2.2 Channel flow with equal wall slip

For the case where $S_+ = S_- =: S$ the stationary solution simplifies to

$$\bar{u}(y) = 2S + 1 - y^2. \quad (15)$$

In this case, Eq. (14) gives

$$(\cos k - Sk \sin k)(\sin k + Sk \cos k) = 0. \quad (16)$$

Using Eq. (16), the formula for the series coefficients A_n can be simplified to

$$A_n = \begin{cases} \frac{4 \sin k_n (\sin k_n + k_n S \cos k_n)}{k_n^3 (k_n^2 S^2 + S + 1)} & \text{for } n \text{ odd} \\ 0 & \text{for } n \text{ even.} \end{cases} \quad (17)$$

We make an argument that Eq. (11) cannot be simplified in this way: We denote the factors in Eq. (14) by A , B , C , and D . It can be shown that only two cases are possible: Either $A = B = C = D = 0$ or $A, B, C, D \neq 0$. In the first case, no k_n can be obtained. Hence, it follows that $B \neq 0$ in general and consequently the former case has to hold from which it follows that $A_n \neq 0$ in general.

Two limit cases arise for the variation of S , which are considered in the following. These are the case for a vanishing slip length, corresponding to the limit $S = 0$ and a diverging slip length leading to $S \rightarrow \infty$. The boundary conditions for the former case are the well known *no slip* conditions, while the latter are often referred to as *free slip* or *perfect slip* conditions.

2.3 No slip boundary conditions

For $S = 0$, the boundary conditions Eq. (7) reduce to $u = 0$ at $y = \pm 1$, which are the no slip boundary conditions that are typically used for liquid wall interactions on the macroscopic scale. This allows to reduce the slip solution Eq. (8) to

$$u(t, y) = 1 - y^2 - \sum_{n=1}^{\infty} A_n \sin(k_n(y + 1)) \exp(-k_n^2 t). \quad (18)$$

In contrast to the problem with Navier slip boundary conditions, the coefficients can be *explicitly* computed giving

$$k_n = n\pi/2, \quad n \in \mathbb{N} \quad (19)$$

Thereby, (17) reduces to

$$A_n = \begin{cases} 4/k_n^3 & \text{for } n \text{ odd} \\ 0 & \text{for } n \text{ even.} \end{cases} \quad (20)$$

This solution can, e.g., be found in collections for analytic solutions, such as [5].

2.4 Free slip boundary conditions

For $S \rightarrow \infty$ the Navier slip boundary condition is equivalent to the *free slip* boundary condition

$$\partial_y u = 0 \quad \text{at } y = \pm 1. \quad (21)$$

In this case, it follows from Eq. (17) that $A_n = 0 \forall n \in \mathbb{N}$. Hence, the homogeneous solution of Eq. (5) is identically zero leaving the particular solution of Eq. (5), Eq. (6), and Eq. (7) for $S \rightarrow \infty$

$$u(t, x) = 2t, \quad (22)$$

as solution for the overall problem. Even though this solution does not require the computation of any series coefficients, we note for a later comparison that in this case the solution of the characteristic equation is

$$k_n = n\pi, \quad n \in \mathbb{N}. \quad (23)$$

3 An algorithm for the starting flow with slip boundary conditions

In order to evaluate the series solution Eq. (8) at some point in time and space, it is necessary to obtain the coefficients k_n . We first analyze the properties of Eq. (12) and based on this analysis we give an algorithm that obtains all series coefficients in increasing order.

We consider Eq. (12) for $S_+, S_- \geq 0$ and distinguish two cases for $\cos(2k)$: **Case 1** with $\cos(2k) \neq 0$. In this case we can divide by $\cos(2k)$ and obtain

$$(1 - S_+ S_- k^2) \tan(2k) + k(S_+ + S_-) = 0. \quad (24)$$

Assuming that $k = \frac{1}{\sqrt{S_+ S_-}}$ is a root of Eq. (24) gives the contradiction

$$0 < (S_+ + S_-) / \sqrt{S_+ S_-} = 0. \quad (25)$$

Hence, $k = 1/\sqrt{S_+ S_-}$ is not a root of Eq. (24). A similar argument can be made for $k = (2n + 1)/4\pi$. Based on

$$\Phi = \left\{ 1/\sqrt{S_+ S_-} \right\} \cup \{(2n + 1)\pi/4 \mid n \in \mathbb{N}_0\} \quad (26)$$

we define

$$\begin{aligned} f : \mathbb{R}_+ \setminus \Phi &\rightarrow \mathbb{R} \\ f &\mapsto \tan(2k) + \frac{k(S_+ + S_-)}{1 - S_+ S_- k^2}. \end{aligned} \quad (27)$$

This function is illustrated by the blue line in Fig. 1. The singularities of f are marked by triangles on the x -axis, which corresponds to the elements of Φ . The upward and downward pointing triangles indicate the location of a singularity caused by the tangent-term and the fraction term in Eq. (27), respectively. Hence, the triangles indicate the elements of Φ . The black dots show the locations of the roots of Eq. (27). Between every two points where f is singular, there is a root of f . The inset in Fig. 1 highlights the case where two singularities are nearly coinciding. Note that for such a case, the corresponding root could easily be missed with a manual approach.

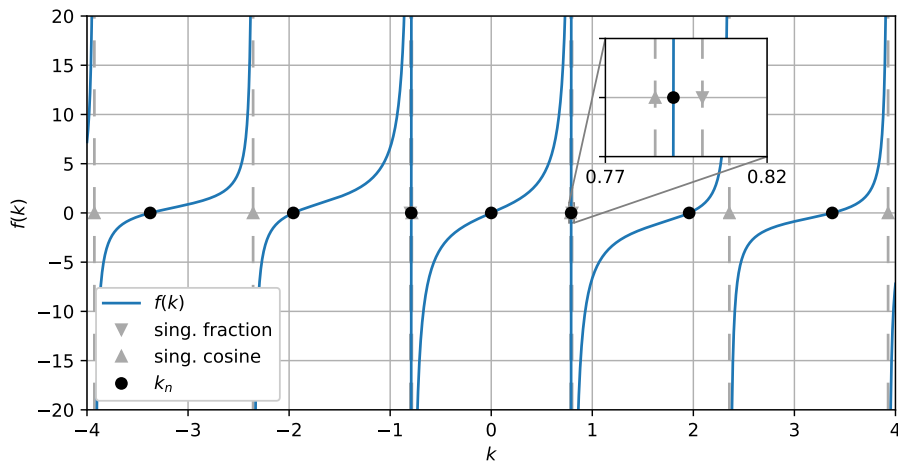


Figure 1: The blue line illustrates the modified characteristic equation Eq. (27) for $S_+ = S_- = 1.25$. The singular points arising from the first and second term of f are marked by upwards and downwards pointing triangles, respectively. The vertical dashed lines mark the location of singularities, while the interval in between two such consecutive points is guaranteed to contain a single zero of f . The black dots show the roots of Eq. (27). The inset shows a root that can easily be missed by a manual coefficient computation.

We note that only $k > 0$ is admissible for the case of the Sturm-Liouville problem leading to Eq. (10), see the Appendix of [16]. As shown above, the set Φ does not contain any roots of the characteristic equation Eq. (12). Hence, in this case, the roots of Eq. (27) are the zeros of Eq. (12). The elements of Φ can be ordered such that

$$0 < \phi_1 < \phi_2 < \dots \quad \forall \phi_n \in \Phi. \quad (28)$$

The function f is strictly monotonic in $\mathbb{R} \setminus \Phi$ as

$$f'(k) = \frac{2}{\cos^2(2k)} + (S_+ + S_-) \frac{1 + S_+ S_- k^2}{(1 - S_+ S_- k^2)^2} > 0 \quad \forall k \in \mathbb{R}_+ \setminus \Phi. \quad (29)$$

Furthermore, we have for all singularities of f :

$$\lim_{k \downarrow \phi_n} f(k) = -\infty \quad \text{and} \quad \lim_{k \uparrow \phi_n} f(k) = \infty \quad \forall n \in \mathbb{N}. \quad (30)$$

As $\mathbb{R}_+ \setminus \Phi$ is open, it follows from Eq. (30) that there exist $a_n, b_n \in (\phi_n, \phi_{n+1})$ such that $f(a_n) < 0$ and $f(b_n) > 0$. Hence, the intermediate value theorem applied to the restricted function $\tilde{f}_n := f|_{[a_n, b_n]}$ guarantees the existence of a root k_n for which $a_n < k_n < b_n$. As f is monotonic so is \tilde{f}_n and consequently the root of \tilde{f} in (ϕ_n, ϕ_{n+1}) is unique. Given the input for the left and right bounds as above the bisection algorithm converges to the root of a strictly monotonic function. A proof of the convergence of the bisection method under the given conditions can be found in [6, chapter 2, p.51, Theorem 2.1].

Case 2 We follow from $\cos(2k) = 0$ that $2k = (2n+1)\pi/2$, $n \in \mathbb{N}_0$, as $k > 0$. In this case, we also have $\sin(2k) = (-1)^{2n+1}$. Plugging these into Eq. (12) leads to

$$k = \frac{2\tilde{n} + 1}{4} \pi = \frac{1}{\sqrt{S_+ S_-}} \quad (31)$$

for some fixed $\tilde{n} \in \mathbb{N}_0$. Hence, this case gives a single coefficient k if and only if the choice of slip lengths satisfies

$$S_+ S_- = \frac{16}{(2\tilde{n} + 1)^2 \pi^2}. \quad (32)$$

Otherwise, this case does not provide any coefficient at all.

Considering Fig. 1, case 2 can be illustrated as follows: If the slip length values are continuously changed, the singularity due to the fraction term in Eq. (27) is moving on the x -axis. When Eq. (32) is satisfied, the singularity due to the fraction term of Eq. (27) is coinciding with one of the singularities cause by the tangent-term, i.e. the downward pointing triangle is located at the same location as one of the upward pointing triangles. Even if Eq. (32) is only approximately satisfied, a root of Eq. (27) is located between nearly coinciding singular points and could easily be missed if the coefficients k_n would be obtained by a manual approach. Note that this case also occurs for the special case $S_+ = S_-$.

To automatically compute all coefficients k_n , we propose the following algorithm:

Algorithm 1 Start-up Coefficient Computation (SCC)

1. Start: Given $S_+, S_- \geq 0$ the algorithm computes the first N coefficients k_1, \dots, k_N . We start by initializing $\tilde{\Phi} = \{(2n+1)\pi/4 \mid n \in \mathbb{N}_0\}$.
2. The index \tilde{n} of the root caused by the fractional term in Eq. (27) is obtained by

$$m := \left(\frac{1}{S_+ S_-} - \left(\frac{1}{S_+ S_-} \bmod \frac{\pi}{4} \right) \right) / \frac{\pi}{4} \quad (33)$$

from which we set

$$\tilde{n} := \begin{cases} (m-1)/2 & \text{if } m \text{ is odd} \\ (m-2)/2 & \text{if } m \text{ is even.} \end{cases} \quad (34)$$

If $\tilde{n} > N$, then $k_{\tilde{n}} > k_N$ and the root caused by the fractional term does not coincide with any of the first N roots and we continue with step 3. Otherwise, based on the considerations for case 2, Eq. (32) is used to identify the case where two singular points of Eq. (27) coincide by

$$|\pi^2 S_+ S_- (2\tilde{n} + 1)^2 - 16| \leq 3 \text{ ulp}. \quad (35)$$

Here ulp is the unit in the last place. If Eq. (35) is not satisfied, we add $1/\sqrt{S_+ S_-}$ to $\tilde{\Phi}$ and continue with the next step. Otherwise, the root with index \tilde{n} is set to $1/\sqrt{S_+ S_-}$ due to Eq. (31) and roots with indices $1, \dots, \tilde{n}-1, \tilde{n}+1, \dots, N$ are computed in the next step.

3. All remaining coefficients are obtained using the bisection method to obtain the unique root k_i of f in the interval (ϕ_i, ϕ_{i+1}) where ϕ are defined in Eq. (28). The initial values for the bisection method

$$a_i := \phi_i + \text{ulp} \quad \text{and} \quad b_i := \phi_{i+1} - \text{ulp} \quad (36)$$

are used.

Roots of Eq. (27) can be located arbitrarily close to singularities, so that in these cases, the precision of the used floating-point arithmetic becomes relevant. Due to the finite floating point precision available on the hardware, we recommend to increase the used floating point precision when required. For this purpose, we provide two different implementations: one using python that is based on a standard double floating point standard and a C++ that provides an arbitrary precision implementation. The C++ implementation is build using the boost multiprecision library.

4 Results

4.1 Verification against arbitrary precise results

A comparison of our results to coefficient values from literature showed that the provided precision is relevant when comparing coefficients for different values for S_+ and S_- . We refer to Section 4.3 for a detailed comparison and take this observation as a motivation to shortly compare between different implementations of our algorithm with respect to their accuracy.

To provide a reliable reference, improve computation speed, and extend the range of applicability of the implementation, the algorithm has been implemented using the C++ programming language in combination with the boost arbitrary precision library. With this implementation, it is possible to compute an arbitrary number of coefficients with an arbitrary accuracy. The two independent implementations (double precision python based and C++-based arbitrary precision) will be compared in the following using the arbitrary precision implementation with 50-significant decimal digits. The APA-bisection method is using a $\text{rTol} = 10^{-40}$, while the double precision implementation is using the scipy default settings. The precision requirement will become more evident in the comparison to literature values further below.

A comparison of absolute and relative errors for k_n^* and A_n^* for $S_+ = S_- = S$ can be seen in Fig. 2 and Fig. 3, respectively. The errors are obtained using the arbitrary precision implementation in C++ as reference. The comparison includes those coefficients for even n to demonstrate that the accuracy of the non-zero coefficients is the same as for those that are analytically zero.

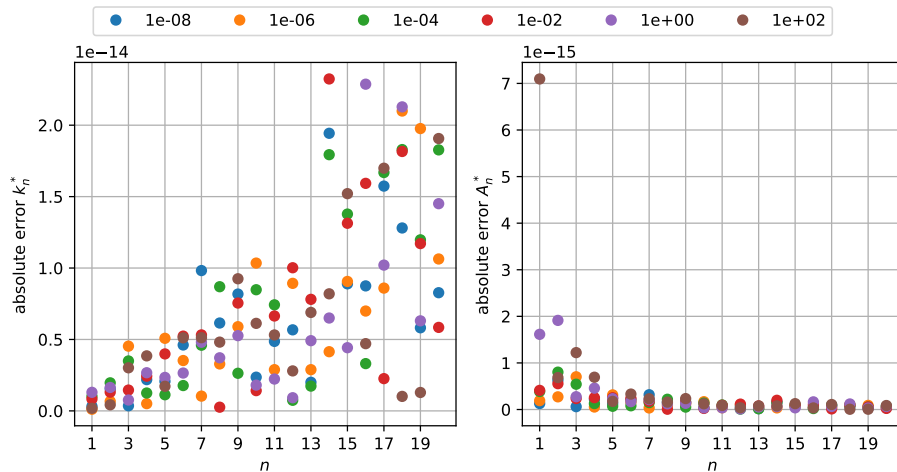


Figure 2: Absolute errors for coefficients from the python implementation for k_n^* and A_n^* for $S = 10^{-8}, 10^{-6}, 10^{-4}, 10^{-2}, 1, 10^2$.

While the absolute errors in Fig. 2 increase for k_n^* with increasing n , the

relative error in Fig. 3 is between 10^{-15} and 10^{-16} for all k_n^* . For the A_n^* -coefficients, the absolute error decreases while the relative error increases with increasing n . The fluctuation of the errors can be explained by an accumulation of round-off and cancellation errors as these values are close to the double precision machine-tolerance.

The computation of the A_n^* coefficients is based on the computation of k_n^* which show a small though positive absolute error. The error for A_n^* is well below 10^{-15} for nearly all coefficients. Furthermore, the trend for the absolute error is inverse to the one for k_n^* as with increasing index the error decreases. This indicates, that the formula for A_n^* is dampening the error introduced by k_n^* .

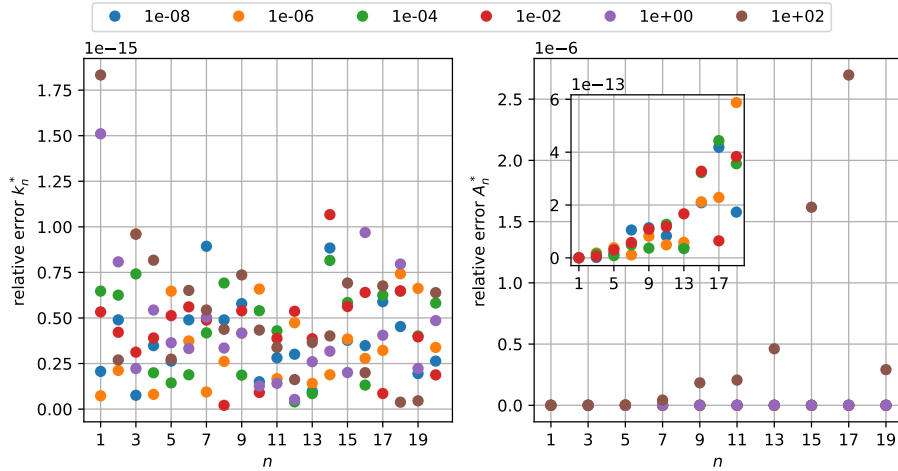


Figure 3: Relative errors of the python implementation for k_n^* and A_n^* for $S = 10^{-8}, 10^{-6}, 10^{-4}, 10^{-2}, 1, 10^2$.

The relative errors for k_n^* are similar to the absolute errors close to machine tolerance and of the same order as for those coefficients that are analytically zero. Again, all errors are on the same order of magnitude - nearly all of them are between 10^{-15} and machine tolerance at 10^{-16} . These errors are satisfactory for the used double precision floating point numbers. The seemingly random distribution is likely due to the round-off errors.

The situation is somewhat different for the relative error for A_n^* depicted in Fig. 2. The relative error for the coefficients corresponding to the case for $S = 100$ show relative errors on the order of 10^{-6} (brown dots). With decreasing S the relative error is on the order of 10^{-13} , which can be seen in the inset in Fig. 3. This behavior can be explained as follows: for increasing S , the coefficients A_n^* quickly decrease in magnitude. Hence, they are barely distinguishable from 0 and further decrease with increasing index number. This behavior makes arithmetic operations between large S and small k_n^* prone to round-off errors.

Based on an accurate computation of k_n^* , the A_n^* -coefficients are obtained and shown in a semi-logarithmic plot in Fig. 4. It can be seen that the results from the python and C++ implementation show excellent agreement. The numerical results for the coefficients with even index are also shown in the plot. As the python implementation is based on a `double` precision, the absolute values for the A_n^* -coefficients are approximately 10^{-16} , which corresponds to machine precision for this case. The results using the arbitrary precision C++-implementation have a relative tolerance of 10^{-40} , which is reflected in results for the coefficients with even index obtained from the C++-implementation.

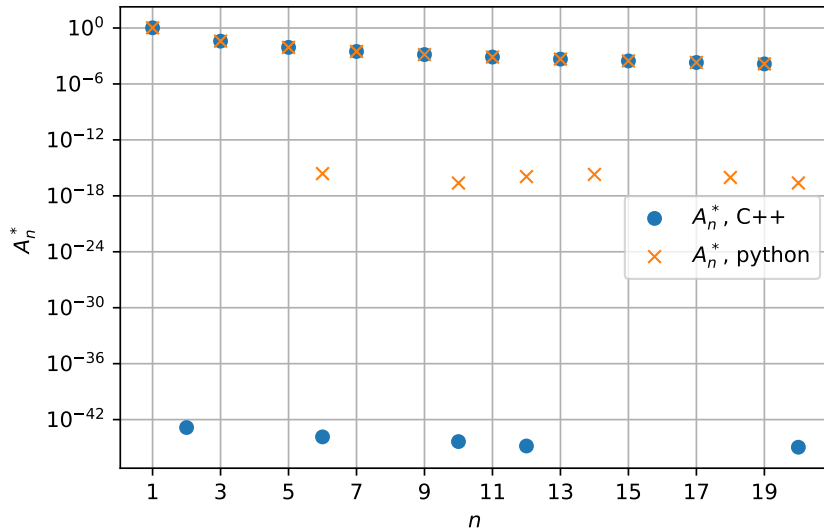


Figure 4: Comparison of A_n^* -coefficients between python and C++ implementation for $S = 10^{-2}$. Python results can be obtained up to an absolute error of 10^{-16} , while the C++ implementation provides results with an error smaller than 10^{-40} . The results for A_n^* reflect this accuracy with absolute values smaller than 10^{-16} and 10^{-40} for the python and C++ implementations, respectively, whereas it follows analytically that $A_{2n}^* = 0 \forall n \in \mathbb{N}$, see Eq. (17).

4.2 Verification of Navier slip boundary conditions

While the comparison in the former section shows an excellent agreement between the two different implementations of the solution algorithm presented in Section 3, this section compares the results of the start-up algorithm to the full direct numerical solution (DNS) of the single phase Navier-Stokes equations between two plates. Here, the fully resolved flow provides an “external” reference solution for the implementation. To solve the single phase Navier-Stokes equations in a channel flow geometry, the CFD-framework OpenFOAM extend

v.3.1 is used. Specifically, the single phase Navier-Stokes solver `icoFoam` is applied for this purpose. In the following, the solutions obtain by the DNS of the Navier Stokes equations are referred to as “CFD-solution”, while the result of the start-up algorithm is referred to as “analytic solution”.

As Eq. (1) neglects the influence of the convection term, we consider a verification case with a vanishing Reynolds number. Furthermore, as the solution depends only on time t and the spacial y -direction, no changes in the velocity field in x -direction have to be expected. Hence, it is sufficient to only resolve the domain in y -direction, where N_y is the number of cells used in the cross section of the channel. As input parameters for the OpenFOAM solver `icoFoam`, we use a kinematic viscosity of $\nu = 0.1 \text{ m}^2 \text{ s}^{-1}$ and a channel height of $H = 1 \text{ m}$.

To demonstrate the applicability of the start-up algorithm for a wide range of parameters, a large variety of slip lengths ranging from $L = 10^{-8}$ to 10^1 m is considered. To analyze the mesh convergence for each of these slip lengths, mesh resolutions between $N_y = 5$ and $N_y = 160$ have been used, where the resolution has been increased by a factor of two each time.

The results of these mesh convergence studies are illustrated in Fig. 5. The velocity field from the analytic solution (ANA) obtained from the start-up algorithm and results from the full numerical solution of the transient Navier-Stokes equations using OpenFOAM (NUM) are compared. The developing velocity fields are shown for two different length scale ratios. The left figure illustrates the case with $S_- = 0.2$ on the left and $S_+ = 2$ on the right wall. The right figure shows results for the case with an equal slip length of $S_+ = S_- = S = 2$. All quantities have been scaled using Eq. (4). The results obtained from the full numerical solution of the velocity field are depicted by empty circles. Note that only a subset of the CFD-solution has been plotted to allow for a better comparison to our solution, which is shown as dashed lines. The different times at which the velocity field is shown is indicated by different colors. The colors repeat periodically with increasing time. The different evaluation times vary between the initial time at $t^* = 0$ to nearly twice the characteristic time of the no slip solution (R^2/ν), which is 2.5 in this case.

Starting from an initially identically zero velocity field, the velocity increases in magnitude over time and converges to the stationary solution (continuous black line). Comparing the two start-up solutions on the left and on the right one can observe the influence of the different slip lengths on the solution. With increasing slip length, the slip at the channel walls at $y = \pm 1$ increases, as well as the maximum velocity in the center of the channel. Both effects contribute to an overall increased volume flux through the channel. Also note that the characteristic time scale increases with increasing S . This effect is further detailed below. Overall, an excellent agreement between numerical and analytical velocity field can be observed for all times including the limit for the stationary solution.

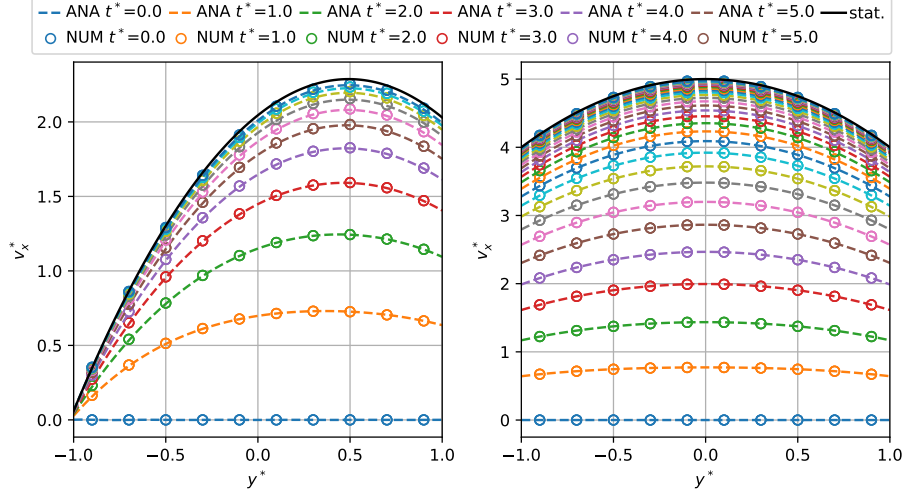


Figure 5: Comparison of non-dimensional results obtained from the analytic solution (ANA) using the start-up algorithm and results from the full numerical solution of the transient Navier-Stokes equations using OpenFOAM (NUM). In the left plot, results for $S_+ = 2$ and $S_- = 0.2$ are shown. The right plots illustrates the case for $S_+ = S_- = 2$. The time interval between two subsequent velocity profiles is 1.0. The first six velocity profiles are labeled in the legend.

A mesh convergence study has been performed for the parameter set described above. An exemplary result for $S_+ = 2 \times 10^{-4}$ and $S_- = 2 \times 10^{-2}$ is shown in Fig. 6. The horizontal axis shows the mesh resolution in the cross section of the channel. The vertical axis depicts the error of the CFD-solution that is defined by

$$e = \|u_{\text{num}} - u_{\text{ana}}\|_{\infty} \quad (37)$$

where u_{num} is the vector containing the velocities in x^* -direction obtained from the CFD-solution and u_{ana} is the vector containing the results of the analytic solution.

The plot contains results for a variety of dimensionless times between $t = 0.5$ and 4.5. Each of the continuous lines corresponds to the mesh convergence for different meshes at a certain dimensionless time. Each dot on the line corresponds to a certain mesh resolution N_y where the error has been computed by applying Eq. (37). A comparison of slope of the error curves to the second order (dashed) reference curve shows a second order convergence of the CFD-results. This is also the expected convergence order based on the choice of the spacial discretization schemes of the CFD-solution. Similar results have been obtained for arbitrary combinations of S_+ and S_- with $S_+, S_- \in \{0, 2 \cdot 10^{-8}, 2 \cdot 10^{-4}, 0.02, 2, 20\}$. Hence, it can be concluded that not only the two implementations of the start-up algorithm are consistent with each

other, but are also consistent with the numerical solution of the full continuum mechanical problem. It should be noted that with increasing S_+ and S_- the problem becomes more challenging for a CFD-solution as required accuracy for the solutions of the involved linear solvers increases.

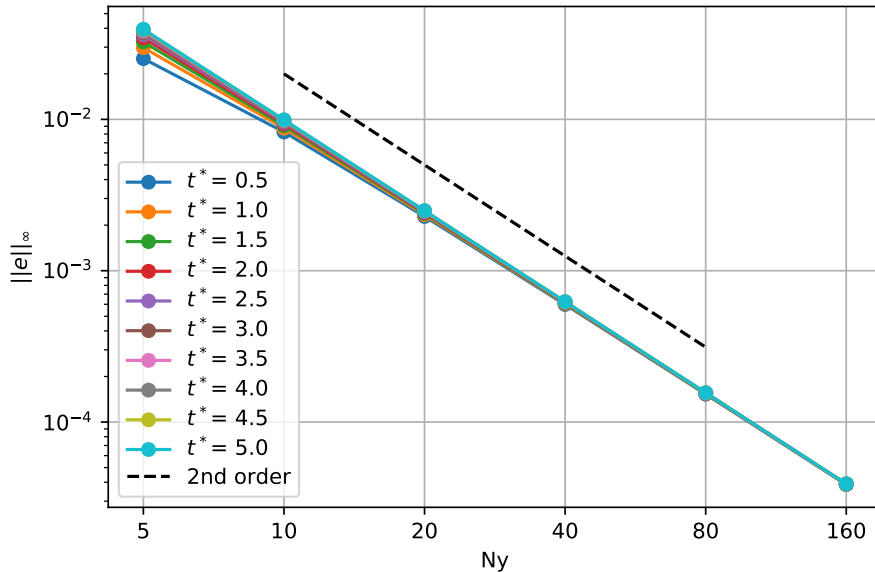


Figure 6: Mesh convergence study using OpenFOAM’s `icoFoam` solver with Navier slip boundary conditions for $S_+ = 2 \times 10^{-4}$ and $S_- = 2 \times 10^{-2}$. The results of the start-up algorithm have been used as analytic reference solution.

4.3 Parameter studies for S_+ and S_-

As discussed in Section 1, the value of the first root of the characteristic equation Eq. (12) is central for a stability analysis of Eq. (5) or the computation of slip lengths from MD-simulations. For such considerations, the dependence of the first root k_1 on S_+ and S_- is a valuable information. This dependence is illustrated in Fig. 7. Without loss of generality (we could switch the placement of S_+ and S_- in Eq. (12)), we place S_+ on the x-axis and use S_- as parameter for different curves. The horizontal axis depicts the variation of S_+ for approximately ten orders of magnitude. The different colored lines show the value of k_1 for different values of S_- . The values for S_- vary between 10^2 and 10^{-2} and have been selected to give a good representation of the k_1 dependence.

Several limit cases can be seen. Firstly, fixing the value for S_- the value for k_1 levels off at a constant value when increasing or decreasing the value of S_+ . Secondly, if S_- is approaching zero, the different curves approach the curve for $S_- = 0$. This limit curve is illustrated by a dashed line in Fig. 7 and represents the maximum for values of k_1^* .

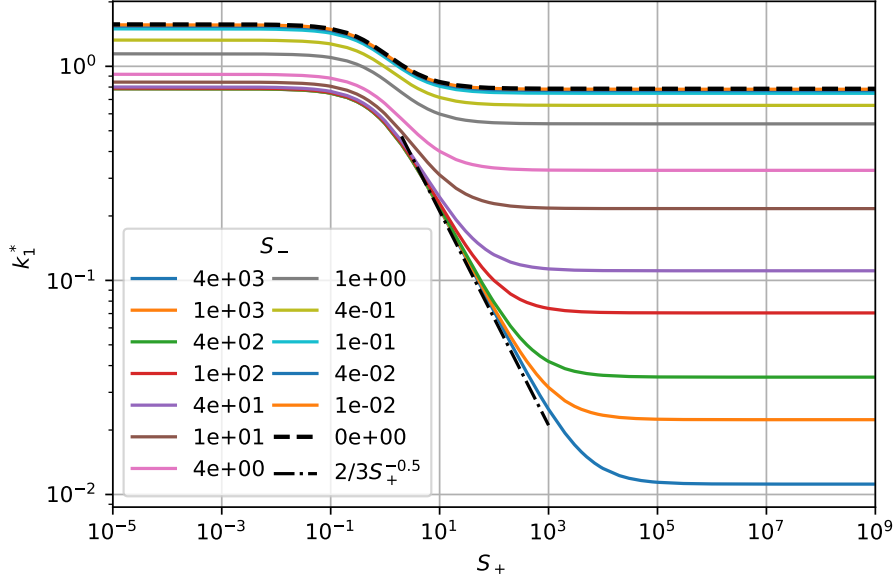


Figure 7: Comparison of the solutions for the first root of (12) by application of Algorithm 1. The horizontal axis depicts the values for S_+ , and the different colors of the curves represent the different values for S_- .

All curves show a transition region between their two limit values that begins at $S_+ \approx 10^{-1}$. This transition region increases in width with increasing S_- . In this region and for much greater values of S_- than shown in Fig. 7 we find an excellent agreement with the power law

$$k_1^* = \frac{2}{3} S_+^{-1/2}. \quad (38)$$

This relation is shown by the dash-dot line in Fig. 7 and the transition region is well described by this relation for all curves with $S_- > 10$.

While Fig. 7 illustrates the dependence of k_1 on the values of S_+ and S_- it is also interesting to compare our results to values available coefficient values for the case $S_+ = S_- = S$. Fig. 8 shows a comparison of the scaled series coefficients for S which are varied by approximately seven orders of magnitude. The plot only depicts those coefficients that are relevant for the computations of the non-zero A_n -coefficients. Plotting the coefficients in this way gives the false impression of a linear relation between the index and the value of the coefficient.

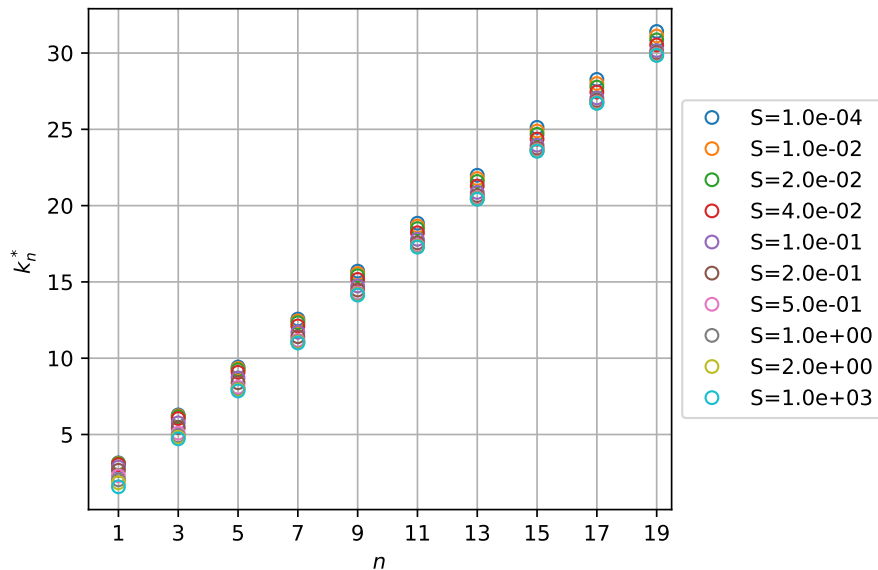


Figure 8: Comparison of the coefficients k_n^* for various ratios S of slip length to channel semi-diameter. Using the scaling from [16] gives a false impression of linearity.

To improve the comparison, the coefficients are scaled using

$$k_n^{**} = (n\pi/2 - k_n^*)/(\pi/2) = n - 2k_n R/\pi. \quad (39)$$

Here the dimensionless quantities k_n^{**} , k_n^* and the coefficient k_n (with dimensions) are used. This scaling yields the normalized difference to the coefficients for the no slip solution Eq. (19). Applying this scaling to the results shown in Fig. 8 yields the coefficients as depicted in Fig. 9. The coefficients vary between 0 and 1 as can be expected for a normalized quantity. The line connecting several coefficients does not indicate intermediate values but has been added to group the coefficients for certain values of S . For $S \rightarrow 0$, the coefficients k_n^{**} approach 0, which corresponds to the limit case with no slip Eq. (19). For a diverging S , the coefficients approach unity, which corresponds to the limit case for free slip boundary conditions and therefore Eq. (23). It can be seen that the coefficients and thereby the results are converging to the two limit cases. Furthermore, differences in the solutions are hard to quantify for extremely large or small values of S . Note that the non-uniform variation of S illustrates the sensitivity to a change in S in a range of approximately 10^{-2} to 10^0 .

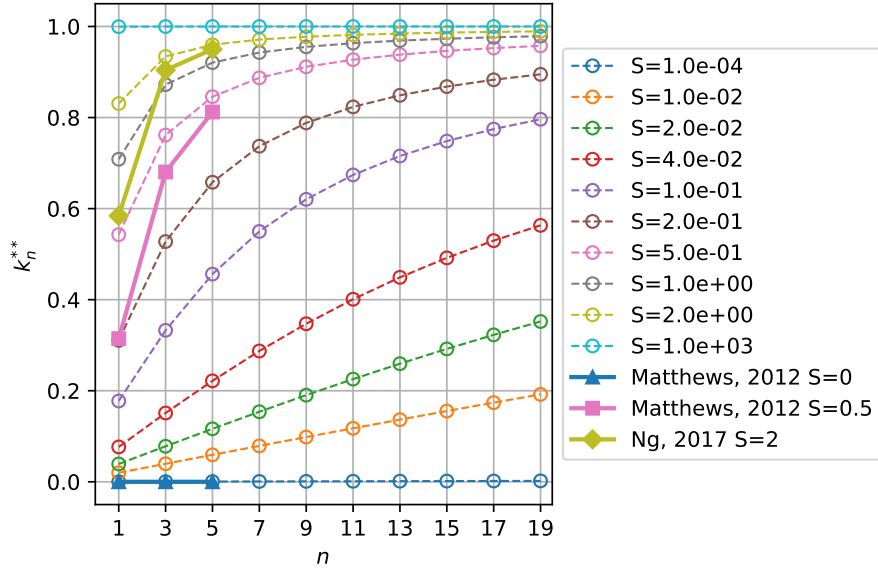


Figure 9: Comparison of the coefficients k_n^{**} for various values of S for the case $S_+ = S_- = S$. The limit cases for the no slip and free slip cases are given by Eq. (19) and Eq. (23), respectively. The lines have been added to guide the eye.

Fig. 9 also shows a comparison to coefficients from literature. In [16] five coefficients are given for $S = 0$ and $S = 0.5$, and in [17] five coefficients are provided for the case $S = 2$. However as $A_n = 0$ if n is even, two of those coefficients are not required for the computation of the velocity field and hence have been omitted in Fig. 9. The coefficients from literature are shown in the same color as the results obtained by the C++-implementation of the start-up algorithm. While the results coincide for the analytically available case $S = 0$, a significant difference for the two other cases $S = 0.5, 2$ can be observed. Even though the results provided in [16, 17] agree with the results obtained here up to the last significant digit, the precision provided in [16, 17] is not sufficient to accurately distinguish between different slip lengths. In this case, the first coefficient for $S = 0.5$ from [16] coincides with the results for $S = 0.2$, with a similar error for the results with $S = 2$ from [17]. For both values a factor of 2.5. However, increasing n , the error decreases.

This observation is particularly noteworthy, as for the computation of the boundary layer thickness from MD results as outlined, e.g., in [8], the resulting computation of the slip length is based on the coefficients with index $n = 1$. Due to this observation, a selection of coefficients for a wide range of values for S is given in Appendix A with 16 significant digits in a normalized floating point format.

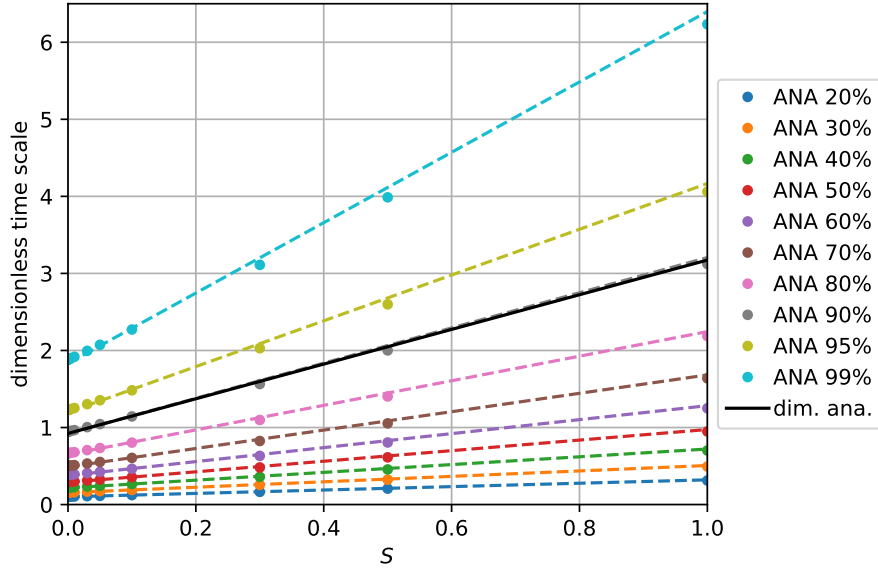


Figure 10: Characteristic relaxation times for startup flow with slip.

As reported in [14, 2, 17, 1], the time scale required to reach a certain fraction of the stationary velocity field increases with increasing slip length on the channel walls. However, these time scales have not been quantified.

Using our algorithm, a parameter study for different values of S has been performed yielding dimensionless times to reach the stationary velocity. Here, we have compared the maximum velocity in the center of the channel. The results of these computations can be seen in Fig. 10. Different characteristic times required to obtain 10% to 99% of the corresponding maximum stationary velocity are shown in dependence of S . Note that the graphs for 10% to 90% subsequently increase by 10%, while the remaining two plots are for 95% and 99%.

The characteristic times for the start up flow without slip, are those for $S = 0$ where the lines for the different time scales intersect with the y -axis. For the no slip case, the characteristic time is approximately 1. This is the time scale needed to reach 90% of the maximum velocity. A dimensional analysis for the time scale yields

$$t_{\text{char}} = C \frac{GR^2}{\mu} S + b \quad (40)$$

as a relation between the dimensionless slip length S and the characteristic time. Using the $b = 0.94$ from the no-slip case and setting $C = 0.9$ gives the function indicated by the black line in Fig. 10. Using least squares for a linear interpolation function gives the dashed lines in Fig. 10. Often, the 90 and 99-percentile cases are of interest. For the values, a least square interpolation of

the data in Fig. 10 gives

$$t_{\text{char},90\%}(S) = 2.16S + 0.94 \quad (41)$$

$$t_{\text{char},99\%}(S) = 4.32S + 1.87. \quad (42)$$

This allows for an arbitrary case to directly estimate the characteristic times by evaluation of Eq. (41) or Eq. (42) for the corresponding value of S .

5 Conclusion

Navier slip boundary conditions are applied to wide variety of different flow problems and analytic solutions for corresponding cases are relevant, among others, to slip length computation from MD-results or as reference solutions for CFD-solvers.

An algorithm has been presented that provides an automated and robust solution to compute the required coefficients for the general case of different slip lengths on the channel walls from the corresponding non-linear characteristic equation. Two implementations, one limited to double-precision and one that can provide arbitrarily accurate results are presented. A comparison confirms that both implementations deliver the same results up to standard double precision machine tolerance. Furthermore they are consistent with the full direct numerical solution of the underlying hydrodynamic problem. The arbitrary precision implementation can provide benchmark results with arbitrary accuracy even for cases with extremely small or large ratios between the slip length and the channel height. Based on the new algorithm a power law for the first series coefficient has been found. This coefficient is essential for slip length computation from MD results and the stability of the series solution. Overall results show that a certain precision is necessary to accurately distinguish between different slip lengths.

The algorithm can be conveniently used as a black box, meaning that no additional work of the user is required for the computation of the coefficients. This replaces the tedious and error prone manual solution, especially in the case of nearly coinciding singularities.

Acknowledgements

Funded by the Deutsche Forschungsgemeinschaft (DFG, German Research Foundation) – Project-B02 265191195 – SFB 1194. Calculations for this research were conducted on the Lichtenberg high performance computer of the TU Darmstadt.

A Reference coefficients

The following tables provide highly accurate results for the coefficients k_n^* and A_n^* computed with the arbitrary precision arithmetic implementation introduced above. For each table, the row gives the corresponding value of S between 10^{-9} and 10^2 , while the column gives the value of the coefficient with indices between 1 and 19. The values are provided for the first 17 digits with rounding to nearest. These results are expected to be sufficiently accurate for a computation with standard double-precision. Coefficients for which analytically $A_n^* = 0$ have been omitted. Note that the coefficients can also be used for the computation of a starting Couette flow as noted in [17].

Table 1: Coefficients k_n^* for different length ratios S , part 1.

	1	3	5	7	9
1e-09	1.5707963252241004e00	4.7123889756723010e00	7.8539816261205013e00	1.0995574276568702e01	1.4137166927016903e01
1e-08	1.5707963110869334e00	4.7123889332608009e00	7.8539815554346672e00	1.0995574177608535e01	1.4137166799782401e01
1e-07	1.5707961697152797e00	4.7123885091458391e00	7.8539808485763984e00	1.0995573188006958e01	1.4137165527437517e01
1e-06	1.5707947560001405e00	4.7123842680004220e00	7.8539737800007030e00	1.0995563292000984e01	1.4137152804001266e01
1e-05	1.5707806189887081e00	4.7123418569661553e00	7.8539030949436954e00	1.0995464332921390e01	1.4137025570899302e01
1e-04	1.5706392628699011e00	4.7119177886406973e00	7.8531963145044754e00	1.0994474840523223e01	1.4135753366758927e01
1e-03	1.5692271009819729e00	4.7076813338280239e00	7.8461356593167482e00	1.0984590139197781e01	1.4123044835202544e01
1e-02	1.5552451292561666e00	4.6657651417272481e00	7.7763740778469526e00	1.0887130102147713e01	1.3998089735155082e01
1e-01	1.4288700112140771e00	4.3058014131192230e00	7.2281097716272491e00	1.0200262588295905e01	1.3214185683842919e01
1e00	8.6033358901937973e-01	3.4256184594817283e00	6.4372981791719468e00	9.5293344053619631e00	1.2645287223856643e01
1e01	3.1105284820029772e-01	3.1730971766928695e00	6.2990593598956464e00	9.4353759757608469e00	1.2574323161037869e01
1e02	9.9833638551126355e-02	3.1447725231101660e00	6.2847764523279794e00	9.4258388739020980e00	1.2567166338520057e01

Table 2: Coefficients k_n^* for different length ratios S , part 2.

	11	13	15	17	19
1e-09	1.7278759577465102e01	2.0420352227913305e01	2.3561944878361505e01	2.6703537528809704e01	2.9845130179257907e01
1e-08	1.7278759421956270e01	2.0420352044130137e01	2.3561944666304001e01	2.6703537288477868e01	2.9845129910651735e01
1e-07	1.7278757866868077e01	2.0420350206298636e01	2.3561942545729195e01	2.6703534885159755e01	2.9845127224590314e01
1e-06	1.7278742316001548e01	2.0420331828001832e01	2.3561921340002115e01	2.6703510852002395e01	2.9845100364002679e01
1e-05	1.7278586808877492e01	2.0420148046856024e01	2.3561709284834961e01	2.6703270522814361e01	2.9844831760794289e01
1e-04	1.7277031893273573e01	2.0418310420129149e01	2.3559588947387645e01	2.6700867475111043e01	2.9842146003361329e01
1e-03	1.7261499809036966e01	2.0399955122374212e01	2.3538410836847422e01	2.6676867014042465e01	2.9815323715490695e01
1e-02	1.7109307259726943e01	2.0220834187410407e01	2.3332718796715039e01	2.6445005751843368e01	2.9557735806876639e01
1e-01	1.6259361225504154e01	1.9327034291602711e01	2.2410848328443429e01	2.5506382988977435e01	2.8610581936555896e01
1e00	1.5771284874815882e01	1.8902409956860023e01	2.2036496727938566e01	2.5172446326646664e01	2.8309642854452012e01
1e01	1.5714326801776345e01	1.8854859544307704e01	2.1995694888011272e01	2.5136719451598626e01	2.8277870201784616e01
1e02	1.5708599861836207e01	1.8850086423035542e01	2.1991603294103655e01	2.5133139109756151e01	2.8274687555520739e01

Table 3: Coefficients A_n^* for different length ratios S , part 1.

	1	3	5	7	9
1e-09	1.0320491039264819e00	3.8224040886165996e-02	8.2563928314118538e-03	3.0088895158206464e-03	1.4157052180061476e-03
1e-08	1.0320491225033654e00	3.8224041574198647e-02	8.2563929800268752e-03	3.0088895699806220e-03	1.4157052434888137e-03
1e-07	1.0320493082721889e00	3.8224048454517968e-02	8.2563944661726216e-03	3.0088901115771622e-03	1.4157054983129653e-03
1e-06	1.0320511659590730e00	3.8224117256988932e-02	8.2564093271836596e-03	3.0088955272211137e-03	1.4157080463036414e-03
1e-05	1.0320697426929779e00	3.8224805209473876e-02	8.2565578926514244e-03	3.0089496515156807e-03	1.4157335011263999e-03
1e-04	1.0322554965384569e00	3.8231677511858519e-02	8.2580390830709390e-03	3.0094876799708495e-03	1.4159855409592672e-03
1e-03	1.0341116856423846e00	3.8299678307806458e-02	8.2724045924216522e-03	3.0145465588273398e-03	1.4182551555536466e-03
1e-02	1.0525387018317054e00	3.8907643838938369e-02	8.3717196531905725e-03	3.0334116162406537e-03	1.4164048125480716e-03
1e-01	1.2237769119142639e00	3.8981626729527902e-02	6.5284927034244883e-03	1.7608409260036317e-03	6.0908996408140775e-04
1e00	2.2923516074712986e00	7.2446719680633780e-03	3.4520033975000920e-04	4.9806482610557783e-05	1.2218509338424761e-05
1e01	6.4284132507787826e00	1.2300539013759826e-04	4.0223434904942518e-06	5.3422924776366766e-07	1.2715541771687607e-07
1e02	2.0033283427296421e01	1.2991835173483862e-06	4.0784935589731436e-08	5.3753972617863454e-09	1.2759845080602730e-09

Table 4: Coefficients A_n^* for different length ratios S , part 2.

	11	13	15	17	19
1e-09	7.7539376703717627e-04	4.6975380242443397e-04	3.0579232708932778e-04	2.1006495093150440e-04	1.5046640966999284e-04
1e-08	7.7539378099424116e-04	4.6975381087998306e-04	3.0579233259357290e-04	2.1006495471265872e-04	1.5046641237837497e-04
1e-07	7.7539392056283482e-04	4.6975389543373275e-04	3.0579238763451399e-04	2.1006499252286892e-04	1.5046643946100329e-04
1e-06	7.7539531604319716e-04	4.6975474079711627e-04	3.0579293789293681e-04	2.1006537049169286e-04	1.5046671016800416e-04
1e-05	7.7540925028942885e-04	4.6976317701963175e-04	3.0579842537832575e-04	2.1006913685210369e-04	1.5046940530977386e-04
1e-04	7.7554653701934284e-04	4.6984579812085834e-04	3.0585179035765763e-04	2.1010546768392832e-04	1.5049516391538000e-04
1e-03	7.7671389919512998e-04	4.7049797723244872e-04	3.0623454555781676e-04	2.1033560400141092e-04	1.5063358634863930e-04
1e-02	7.6848100398766675e-04	4.6036920630577967e-04	2.9582993679644034e-04	2.0027735474255085e-04	1.4115459236280014e-04
1e-01	2.4857199236583632e-04	1.1458746030383859e-04	5.8044230570411602e-05	3.1693557376343359e-05	1.8393628921613791e-05
1e00	4.0667411118106691e-06	1.6483518052363482e-06	7.6658838066193622e-07	3.9451567742351955e-07	2.1943484795376281e-07
1e01	4.1724166865955799e-08	1.6780663383512985e-08	7.7673491366614353e-09	3.9851199782459977e-09	2.2119065233304189e-09
1e02	4.1817188411938867e-10	1.6806640809123729e-10	7.7761827471564228e-11	3.9885897807771079e-11	2.2134281658204133e-11

References

- [1] Abou-Dina, M. S. et al. “Newtonian plane Couette flow with dynamic wall slip”. In: *Meccanica* 55 (2020), pp. 1499–1507.
- [2] Avramenko, A. A., Tyrinov, A. I., and Shevchuk, I. V. “An analytical and numerical study on the start-up flow of slightly rarefied gases in a parallel-plate channel and a pipe”. In: *Physics of Fluids* 27.4 (2015), p. 42001.
- [3] Avramenko, A. A., Tyrinov, A. I., and Shevchuk, I. V. “Start-up slip flow in a microchannel with a rectangular cross section”. In: *Theor. Comput. Fluid Dyn.* 29 (2015), pp. 351–371.
- [4] Bestman, A. R., Ikonwa, I. O., and Mbeledogu, I. U. “Transient slip flow”. In: *International Journal of Energy Research* 19.3 (1995), pp. 275–277.
- [5] Brenn, G. *Analytical Solutions for Transport Processes : Fluid Mechanics, Heat and Mass Transfer*. Mathematical Engineering. Berlin, Heidelberg, 2017.
- [6] Burden, R. and Faires, D. *Numerical Analysis*. Ed. by M. Julet. 9th ed. Stratton, Richard, 2010.
- [7] Castellões, F. V. et al. “Transient Analysis of Slip Flow and Heat Transfer in Microchannels”. In: *Heat Transfer Engineering* 28.6 (2007), pp. 549–558.
- [8] Chen, S. et al. “Determining hydrodynamic boundary conditions from equilibrium fluctuations”. In: *Phys. Rev. E* 92.4 (2015), p. 43007.
- [9] Gad-el-Hak, M. “Transport phenomena in microdevices”. In: *ZAMM - Journal of Applied Mathematics and Mechanics / Zeitschrift für Angewandte Mathematik und Mechanik* 84.7 (2004), pp. 494–498.
- [10] Gad-el-Hak, M. “The Fluid Mechanics of Microdevices—The Freeman Scholar Lecture”. In: *Journal of Fluids Engineering* 121.1 (1999), pp. 5–33.
- [11] Gründing, D. “An enhanced model for the capillary rise problem”. In: *International Journal of Multiphase Flows* (2019).
- [12] Huh, C. and Scriven, L. E. “Hydrodynamic model of steady movement of a solid/liquid/fluid contact line”. In: *Journal of Colloid and Interface Science* 35.1 (1971), pp. 85–101.
- [13] John, V. “Slip with friction and penetration with resistance boundary conditions for the Navier–Stokes equations—numerical tests and aspects of the implementation”. In: *Journal of Computational and Applied Mathematics* 147.2 (2002), pp. 287–300.
- [14] Kaoullas, G. and Georgiou, G. C. “Start-up and cessation Newtonian Poiseuille and Couette flows with dynamic wall slip”. In: *Meccanica* 50 (2015), pp. 1747–1760.
- [15] Majumder, M. et al. “Enhanced flow in carbon nanotubes”. In: *Nature* 438 (2005).

- [16] Matthews, M. T. and Hastie, K. M. “An analytical and numerical study of unsteady channel flow with slip”. In: *The ANZIAM Journal* 53.4 (2012), pp. 321–336.
- [17] Ng, C.-O. “Starting flow in channels with boundary slip”. In: *Meccanica* 52.1 (2017), pp. 45–67.
- [18] Qian, T., Wang, X.-P., and Sheng, P. “Molecular hydrodynamics of the moving contact line in two-phase immiscible flows”. In: *eprint arXiv:cond-mat/0510403* (2006).
- [19] Sharipov, F. and Seleznev, V. “Data on Internal Rarefied Gas Flows”. In: *Journal of Physical and Chemical Reference Data* 27.3 (1998), pp. 657–706.
- [20] Shikhmurzaev, Y. D. *Capillary Flows with Forming Interfaces*. 1st ed. Chapman and Hall/CRC, 2008.
- [21] Tretheway, D. C. and Meinhard, C. D. “Apparent fluid slip at hydrophobic microchannel walls”. In: *Physics of Fluids* 14.3 (2002), pp. L9–L12.
- [22] Wang, C. Y. “Flow over a surface with parallel grooves”. In: *Physics of Fluids* 15.5 (2003), pp. 1114–1121.
- [23] Wang, C. Y. “The Starting Flow in Ducts Filled with a Darcy-Brinkman Medium”. In: *Transport in Porous Media* 75.1 (2008), pp. 55–62.
- [24] Yoshimura, A. and Prud’homme, R. K. “Wall Slip Corrections for Couette and Parallel Disk Viscometers”. In: *Journal of Rheology* 32.1 (1988), pp. 53–67.